Design and Analysis of a Mode-Coupler-Based Multimode Multidrop Si Dielectric Waveguide Channel for Sub-THz/THz Interconnect

Xuan Ding, *Member, IEEE*, Hai Yu, *Member, IEEE*, Sajjad Sabbaghi, *Graduate Student Member, IEEE*, and Qun Jane Gu, *Senior Member, IEEE*

***Abstract*— This article presents a *G*-band mode-coupler-based multimode multidrop Si dielectric waveguide (DWG) for sub-terahertz (THz)/THz interconnect. Four types of mode couplers, including E_{11}^y–E_{11}^y, E_{11}^y–E_{21}^y, E_{11}^y–E_{31}^y, and quasi-TEM to E_{11}^y mode couplers, are analyzed, designed, and demonstrated. The quasi-TEM to E_{11}^y coupler is a microstrip line (MSL)-to-DWG transition. E_{11}^y to E_{21}^y and E_{11}^y to E_{31}^y mode couplers with satisfied phase matching enable two more mode transmissions along the same waveguide. The mode-coupling theory, including the coupling coefficient, the coupling efficiency, crosstalk, and bandwidth, is studied and analyzed mathematically and guides the development of a one-side tapered coupler to boost the bandwidth. Tapered structures are employed as the smooth transition between DWG sections and mode filters to minimize the mode interference in (de)multiplexers and as the radiation terminals to reduce the reflection. The measured minimum transition loss is about 5 dB with the 3-dB bandwidth of 143–200, 151–185, and 155–174 GHz for the three modes, respectively, and the measured crosstalks between modes are less than −26 dB. A multimode multidrop sub-THz interconnect system is also demonstrated with CMOS-based transmitters (TXs)/receivers (RXs) and achieves an aggregate data rate of 65 Gb/s and the energy efficiency of 1.6 pJ/b with a bit error rate (BER) of 10^{-12}.**

***Index Terms*— CMOS, data rate, dielectric waveguide (DWG), E_{11}^y, E_{21}^y, E_{31}^y, energy efficiency, *G*-band, interconnect, mode coupler, multidrop, multimode, nanomanufacturing, quasi-TEM, silicon (Si), sub-terahertz (THz), THz.**

I. Introduction

With the ever-increasing data rates, interconnect research has been active over decades for communications in different scenarios, such as inter/intra-data centers, inter-rack, inter-board, and inter-chip [1]. Traditional electrical and optical interconnects face challenges to completely address interconnect issues due to their inherent constraints, such as channel constraints, fabrication complexity, and environment sensitivity [2]. It then inspires the studies of wireline links [3], [4] at millimeter-wave (mm-wave) and terahertz (THz) because of the broad bandwidth, low loss, and compact size. Sub-THz/THz interconnect also leverages recent great developments in THz technologies, including materials, components, semiconductor devices, packaging processes, and integrated circuit (IC) design [5]. High-resistivity Si ($\varepsilon_r = 11.7$ and $\tan\delta = 0.003$ [6]) with features of high permittivity, low material loss, and main-stream process compatibility enables novel components and system demonstrations based on Si dielectric waveguides (DWGs) [7], [8].

In the past decade, single-channel transmission has great advancements [9], [10], [11], [12], [13]. To further increase bandwidth density without overly stressing active devices and facing challenging dispersion issues, channelization where multiple logical channels share the same physical link is needed. A "data bus," which supports multiple logical channels, not only increases the aggregate data rates, but also provides data communications among distributed nodes, such as chips, boards, and racks, to realize multidrop architecture. To support channelization, there are five main dimensions of multiplexing: time, frequency, space, polarization, and quadrature [14]. In time and quadrature dimensions, signal processing techniques, such as pulse shaping and high-order quadrature modulations, are usually introduced to pack up bit sequences into symbols to reduce the required bandwidth for high spectrum efficiency. However, the corresponding complex systems, including high-signal fidelity synthesizers, high data rate analog-to-digital converter (ADC) and digital-to-analog converter (DAC), and so on, face challenges to be energy efficient and become increasingly worse with higher carrier frequencies, such as sub-THz/THz.

One of the challenges in multichannel sub-THz/THz interconnect lies in the realization of compact and low-loss multiplexers [15]. In [16], a bidirectional plastic waveguide in *E*-band is implemented and achieves 13-dB insertion loss and lower than −55-dB crosstalk. However, the connector is difficult to realize dense interconnects due to its large dimension. Another nonnegligible issue is the interference: when unshielded DWGs get closer, and the coupling becomes considerable. Multiport interconnect consisted of DWG Y-junctions is an option for multicasting and broadcasting in chip-to-chip communications [17], but it does not improve data rates and a 3-dB signal loss is added theoretically with every doubled number of ports. Frequency division multiplexing (FDM) has emerged in waveguide [9], [18], on chip [19], and on substrate [20], to obtain a large total bandwidth for data transmission, but the common section should cover the entire frequency range of all the channels,

Manuscript received 9 May 2023; revised 19 June 2023; accepted 21 June 2023. This work was supported in part by the National Science Foundation (NSF) under Award ECCS-1932821. *(Corresponding authors: Xuan Ding; Qun Jane Gu.)*

The authors are with the Department of Electrical and Computer Engineering, University of California at Davis, Davis, CA 95616 USA (e-mail: xxding@ucdavis.edu; jgu@ucdavis.edu).

Color versions of one or more figures in this article are available at https://doi.org/10.1109/TMTT.2023.3290189.

Digital Object Identifier 10.1109/TMTT.2023.3290189

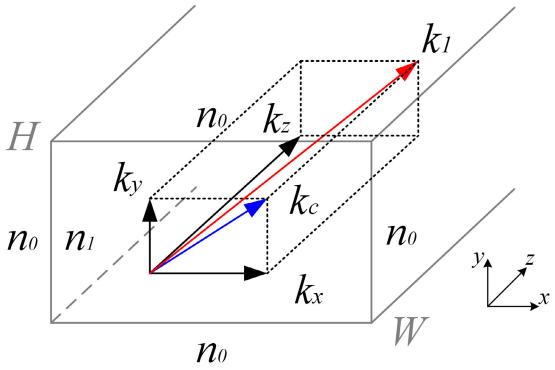

Fig. 1. Wavenumber representation in a rectangular coordinate.

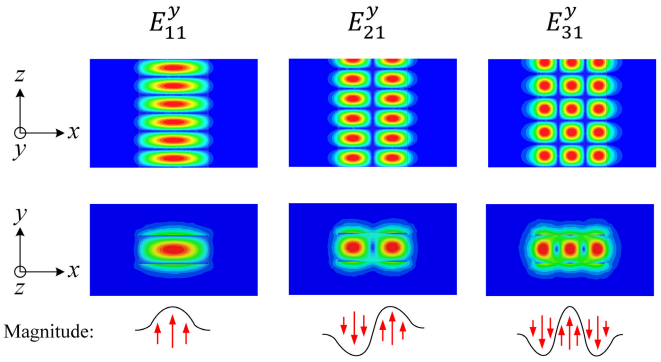

Fig. 2. E-field distribution and magnitude of E_{11}^y, E_{21}^y, and E_{31}^y modes in a multimode rectangular DWG.

thus increasing the design challenges. Polarization multiplexing (orthomode) in [21] and [22] provides two simultaneous channels to double the bandwidth density. However, this approach does not provide ready scaling approach for a larger number of channels.

This article proposes a mode-coupler-based multidrop Si DWG channel with mode division multiplexing (MDM). Multiple mode couplers, such as E_{11}^y–E_{11}^y, E_{11}^y–E_{21}^y E_{11}^y–E_{31}^y, and quasi-TEM to E_{11}^y mode couplers, are analyzed, designed, and demonstrated with rectangular DWGs. The sub-THz interconnect based on the proposed multidrop Si DWG channel has great scalability for larger channel numbers and multidimensions. This article is organized as follows. Section II analyzes the mode-coupler working mechanism, including coupling coefficient, coupling efficiency, crosstalk, bandwidth, and a new one-side tapered coupler. Section III discusses design, optimization, fabrication, and assembling of the multidrop Si channel and system. Section IV presents the multimode multidrop Si DWG channel measurements and system demonstrations of the sub-THz interconnect based on the proposed Si DWG channel. A conclusion is drawn in Section V.

II. Multimode Si DWG Analysis

Even though the electromagnetic (EM) simulators, such as high-frequency structure simulator (HFSS) and computer simulation technology (CST), are powerful, it is still important and beneficial to model passive structures and evaluate their performance theoretically to build up design insights. The study of the multimode DWG and mode coupler with EM theory in this section helps to better understand the working mechanisms and improvement strategies of mode coupling, including coupling coefficient and efficiency, crosstalk, bandwidth of mode couplers, and a new one-side tapered coupler, especially the latter is the first time to elaborate mathematically.

A. Rectangular Multimode DWG

In physics, the propagation characteristics of EM waves, such as direction, period, and velocity, can be described with wavenumbers in a 3-D coordinate. Wavenumber is the spatial frequency of a wave, measured in the phase change per unit distance. Fig. 1 illuminates the wavenumbers and their relationship of EM waves in a rectangular coordinate, assuming the z-axis is the propagation direction in an infinite length, and they can be calculated by the equations below

$$\begin{cases} k_z = \beta = n_{\text{eff}} \cdot k_0 = n_{\text{eff}} \cdot \dfrac{\omega}{c} \\ |k_c| = \sqrt{k_x^2 + k_y^2} = \sqrt{k_1^2 - k_z^2} = \sqrt{n_1^2 k_0^2 - k_z^2} \end{cases} \tag{1}$$

where ω is the angular frequency and c is the light velocity in vacuum. k_0 and k_1 are the wavenumbers in vacuum and medium with a refractive index of n_1, respectively. k_x, k_y, and k_z are the wavenumber components along the x-, y-, and z-axes, in which k_z is also named propagation constant β. k_c is the transverse wavenumber that is the combination of k_x and k_y, and determines the mode orders together with the geometry of the waveguide. The characteristics of an EM wave in a waveguide are also determined by the dielectric medium and boundary conditions. It is significant for an unshielded DWG to confine the EM wave, because the angle φ between k_1 and waveguide boundary should not exceed $\pi/2 - \theta_c$, in which $\theta_c = \arcsin(n_0/n_1)$ is the critical angle, for the total internal reflection. Selecting the dielectric media with proper electrical properties and geometry dimensions is crucial in multimode DWG design.

The fundamental mode E_{11}^y is the lowest y-polarization mode, and there is only one E- and H-field peak along both the x-axis and y-axis directions. To enable higher-order modes in a DWG, the product $k_x W$ (or $k_y H$) must be increased, but k_x (or k_y) cannot increase too much due to the constraint of the critical angle for the total internal refraction condition. Increasing the cross-sectional width W (or height H) is an effective way to allow higher-order modes in a DWG. The width and height determine the highest order along the x-axis and y-axis directions, respectively. Fig. 2 shows a multimode Si (refractive index $n_1 = 3.42$) DWG with air (refractive index $n_0 = 1$) cladding, in which multiple y-polarization modes (e.g., E_{11}^y, E_{21}^y, and E_{31}^y) can exist simultaneously. Their E-field profiles and magnitudes at 165 GHz are plotted in the figure as well. The dimensions of the cross section are $W \times H = 1200 \times 525$ μm.

The effective refractive index, defined as $n_{\text{eff}} = \beta/k_0$, is plotted versus the width W of a Si DWG at 165 GHz, as shown in Fig. 3. It clearly presents that the minimum width for the second-order mode E_{21}^y and third-order mode

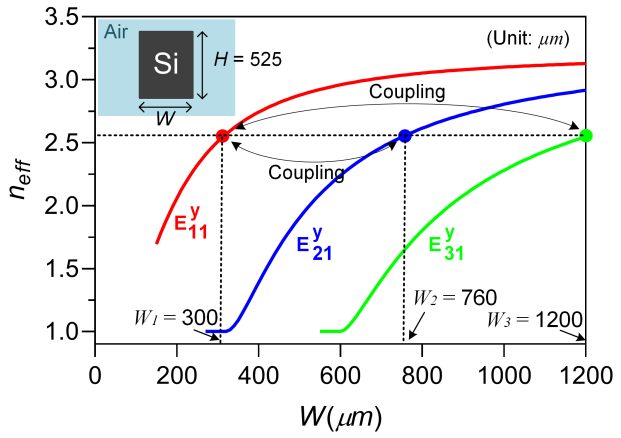

Fig. 3. MATLAB calculated effective refractive index n_{eff} for the three modes (E^y_{11}, E^y_{21}, and E^y_{31}) versus the Si DWG width of W at 165 GHz.

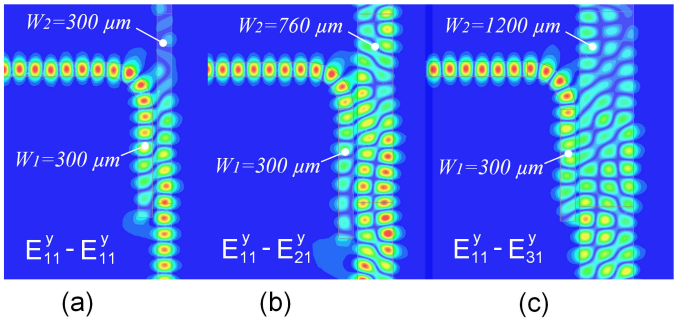

Fig. 4. Configuration and simulated E-field of (a) E^y_{11}–E^y_{11}, (b) E^y_{11}–E^y_{21}, and (c) E^y_{11}–E^y_{31} mode couplers.

E^y_{31} are 330 and 620 μm, respectively. On the other hand, the higher-order modes, such as E^y_{21} and E^y_{31}, can be rejected in a DWG by simply reducing the waveguide width. That is, the operation principle of fiber mode filters to filter out undesired higher-order modes [23]. For a rectangular Si DWG, the n_{eff} and E-field profiles of all the eigen modes can also be solved by the graphic approach [24] at a given frequency. The highest-order mode determines the maximum number of modes that can be supported by a DWG.

B. Mode Coupling and Coupling Coefficient

Two factors are needed for mode coupling: EM field overlap and phase matching. Field overlap means DWGs are close enough, so that the EM fields of adjacent waveguides are interacting; phase matching requires that the propagation constant β is equal for the coupling modes for maximum coupling efficiency. As shown in Fig. 3, by precisely controlling the width of DWG, the n_{eff} of a specific mode can be finely tuned; then, it is possible to make two modes phase matched according to (1). The waveguide width of 300, 760, and 1200 μm is selected for the DWG mode couplers to equal the effective refractive index n_{eff}, then making the coupling modes in the same propagation constant β. Fig. 4 presents three DWG mode couplers for E^y_{11}–E^y_{11}, E^y_{11}–E^y_{21}, and E^y_{11}–E^y_{31} modes. The E-field depicts successful mode coupling at 165 GHz when the phase matching condition is satisfied.

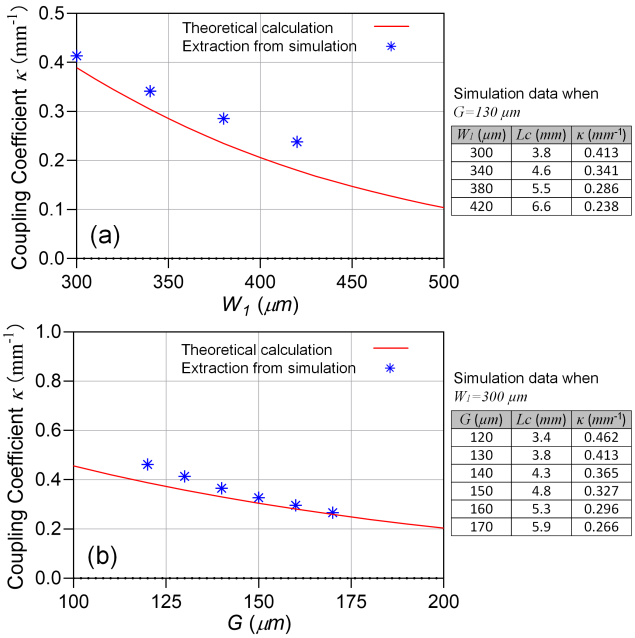

Fig. 5. Calculated and simulated coupling coefficient versus the waveguides' (a) width of W and (b) gap of G.

For a mode coupler, coupling coefficient is known as the coupling strength, which directly determines the optimum coupler length and maximum coupling efficiency. Besides that, the mathematical expression of coupling coefficient is the guideline to optimize the coupler dimensions, such as the waveguide width and gap between coupler arms. $A(z)$ and $B(z)$ are supposed to be the magnitude of the EM field along the propagation direction (z-axis) in the coupled waveguides, respectively. The derivatives $\mathrm{d}A(z)/\mathrm{d}z$ and $\mathrm{d}B(z)/\mathrm{d}z$ describe the field magnitude changing along the z-axis due to the coupling, and they are decided by the coupling coefficient.

The perturbation theory [25] is made to approximate the coupling coefficient: the total E-field and H-field are the sum of the field in each individual waveguide. The EM field both in DWG mode coupler and in each DWG before coupling should satisfy the Maxwell's equations. The approximation is given by the following equation [26]:

$$\kappa = \frac{\sqrt{2\Delta}}{W_1/2} \frac{(k_x W_1/2)^2 (\alpha_x W_1/2)^2}{(1+\alpha_x W_1/2) v^3} e^{(-\alpha_x G)} \tag{2}$$

where $\Delta = ((n_1^2 - n_0^2)/2n_1^2)^{1/2}$ is the relative refractive index difference between the core and cladding, $v = k_0 n_1 W_1 \sqrt{2\Delta}/2$ is the normalized frequency, and G is the gap between DWGs. $\alpha_x = (\beta^2 + k_y^2 - n_0^2 k_0^2)^{1/2}$ is the equivalent wavenumber out of the Si core and describes the EM field decay ratio. For the planar waves, e.g., E^y_{11}, E^y_{21}, and E^y_{31}, $k_y = 0$, then

$$\begin{cases} k_x = \sqrt{(n_1 k_0)^2 - \beta^2} \\ \alpha_x = \sqrt{\beta^2 - (n_0 k_0)^2}. \end{cases} \tag{3}$$

For a given coupler with specific mode and frequency, β is determined, and the coupling coefficient is majorly affected by two parameters: the DWGs' width of W_1 (W_2 is selected to match $\beta = \beta_1 = \beta_2$ in waveguides 1 and 2) and gap of G

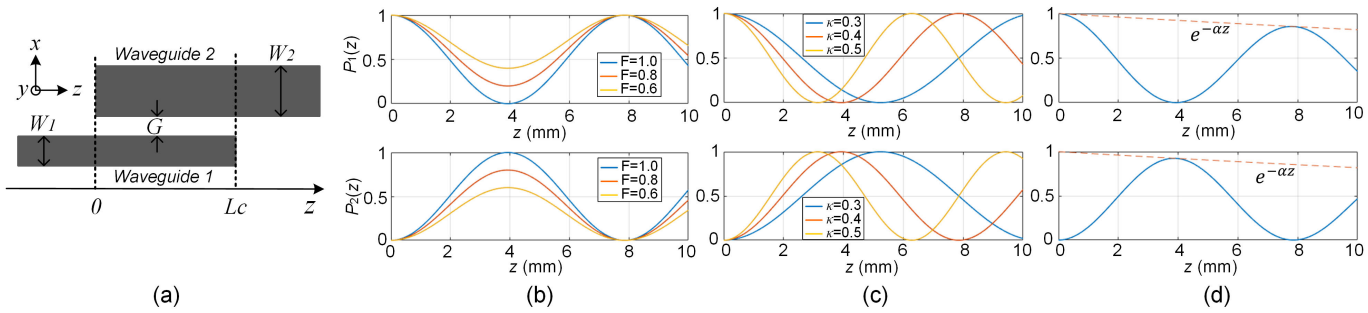

Fig. 6. (a) Geometry illustration of a DWG coupler. Calculated power intensity $P_1(z)$ in waveguide 1 and $P_2(z)$ in waveguide 2 along the z-direction with different coupling efficiency factors F, coupling coefficient κ, and attenuation constant α—(b) $\kappa = 0.4$, $\alpha = 0$, and $F = 0.6, 0.8$, and 1; (c) $F = 1$ ($\delta_\beta = 0$), $\alpha = 0$, and $\kappa = 0.3, 0.4$, and 0.5; and (d) $F = 1$ ($\delta_\beta = 0$), $\kappa = 0.4$, and $\alpha = 0.02$.

between the waveguides. Fig. 5 presents the verification and comparison between the theoretical calculation-based equation (2) and HFSS simulations. The coupling coefficient cannot be extracted directly from the EM solver, but it is inversely proportional to the optimum coupler length L_C according to (8), which will be discussed in Section II-C. In Fig. 5(a), the coupling coefficient is calculated and simulated versus the width of W with a fixed gap of $G = 130$ μm. In Fig. 5(b), the coupling coefficient is plotted when sweeping the gap of G between the coupler arms with a constant width of $W_1 = 300$ μm. The simulation results match the calculation curves very well when the gap is relatively large (compared with the width). However, in small gap, the field superposition assumption is not accurate due to the strong EM field interaction between waveguides, thus causing discrepancy in calculation and simulation. Considering higher-order mode conversion and fabrication capabilities, small gaps should be avoided in this design, and the typical value is in the range of 120–170 μm.

C. Mode-Coupling Efficiency

Coupling efficiency quantifies the power percentage coupled from waveguide 1 to waveguide 2 and determines the insertion loss of the mode coupler. Equation (4) establishes the relation between the EM field magnitude $A(z)$ and $B(z)$, coupling coefficient κ, and propagation constant difference $\delta_\beta = (\beta_2 - \beta_1)/2$, which also explains how the EM field magnitude $A(z)$ and $B(z)$ changes according to the current field strength, κ and δ_β [26]

$$\begin{cases} \dfrac{dA(z)}{dz} = -j\kappa B(z)e^{[-j2\delta_\beta z]} \\ \dfrac{dB(z)}{dz} = -j\kappa A(z)e^{[j2\delta_\beta z]}. \end{cases} \tag{4}$$

The coupling starts where DWGs overlap at $z = 0$, as shown in Fig. 6(a). The initial condition with a normalized magnitude of one is concluded in the following equation:

$$\begin{cases} A(0) = 1, & z = 0 \\ B(0) = 0, & z = 0. \end{cases} \tag{5}$$

For a uniform-width DWG couplers, the width and gap are constant along the z-axis, so κ and δ_β are considered to be independent of z. It is possible to solve the derivative equations with analytical solutions from (4) and (5). One solution of $A(z)$ and $B(z)$ that satisfy the physical characteristics is given in [26].

Then, the power percentage left in waveguide is calculated

$$\begin{aligned} P_1(z) &= \frac{|A(z)|^2}{|A(0)|^2} \\ &= \cos^2\left(\sqrt{\kappa^2 + \delta_\beta^2}z\right) + \frac{\delta_\beta^2}{\kappa^2 + \delta_\beta^2}\sin^2\left(\sqrt{\kappa^2 + \delta_\beta^2}z\right). \end{aligned} \tag{6}$$

Also, the power percentage coupled to waveguide 2, defined as the coupling efficiency η for the desired mode, is obtained

$$\eta = P_2(z) = \frac{|B(z)|^2}{|A(0)|^2} = \frac{\kappa^2}{\kappa^2 + \delta_\beta^2}\sin^2\left(\sqrt{\kappa^2 + \delta_\beta^2}z\right) \tag{7}$$

where a coupling efficiency factor $F = \kappa^2/(\kappa^2 + \delta_\beta^2)$ is defined to evaluate the achievable maximum coupling efficiency, and it is determined by the ratio of δ_β^2/κ^2. The maximum coupling efficiency can reach 1 if the phase is perfectly matched ($\delta_\beta^2 = 0$), as shown in Fig. 6(b).

For an ideal DWG coupler, in which material loss and radiation are ignored, the total power along the propagation direction z-axis is constant. In Fig. 6(c), the maximum η occurs when

$$z = L_C = \frac{\pi}{\sqrt{\delta_\beta^2 + \kappa^2}}\left(m + \frac{1}{2}\right), \quad m = 0, 1, \ldots, \infty. \tag{8}$$

For most of practical scenarios, there is an attenuation constant α existing in practice, and the total power dissipates along the DWG and coupler, as shown in Fig. 6(d). The attenuation constant can be calculated with the loss tangent ($\tan\delta$) of the dielectric material by [27]

$$\alpha = \frac{\omega}{c}\sqrt{\frac{\varepsilon_r'}{2}\left(1 + \tan^2\delta\right) - 1} \tag{9}$$

where ε_r' is the real part of the relative dielectric constant. The $\tan\delta$ of 0.003 for high-resistivity Si at G-band and a coupler length of 3.8 mm selected for the center frequency are utilized to estimate the material loss in the following calculations. The coupling efficiency is expressed as follows if considering the

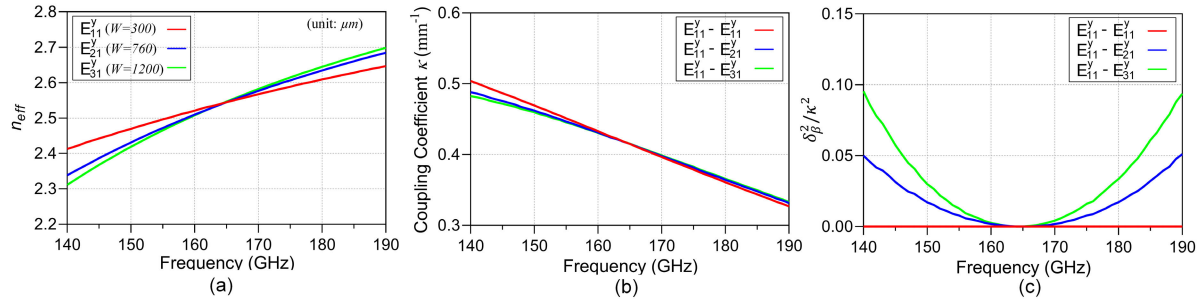

Fig. 7. Frequency-dependent parameters of the DWG and mode coupler for the three different modes with different DWG widths—(a) effective refractive index n_{eff}, (b) coupling coefficient κ, and (c) δ_β^2/κ^2, which is the only determining variable in the coupling efficiency factor F theoretical representation.

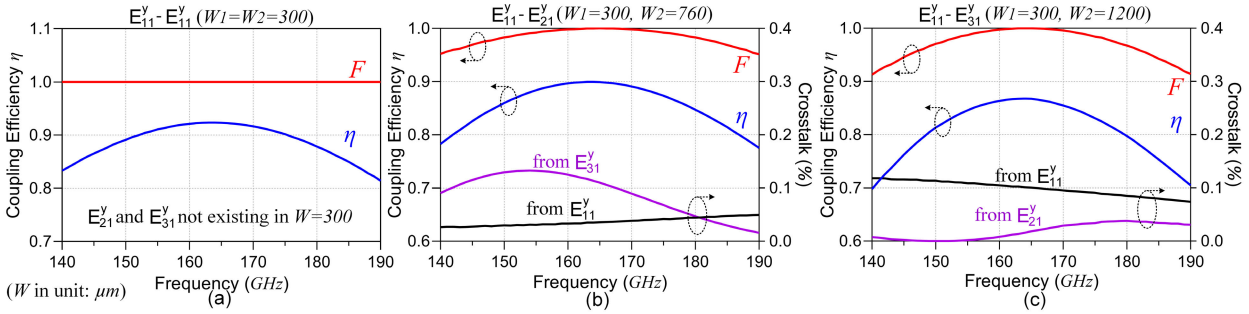

Fig. 8. Calculated coupling efficiency η, coupling efficiency factor F, and mode crosstalk for (a) E_{11}^y–E_{11}^y, (b) E_{11}^y–E_{21}^y, and (c) E_{11}^y–E_{31}^y mode couplers.

material attenuation constant:

$$\eta = \frac{\kappa^2}{\kappa^2 + \delta_\beta^2} \sin^2\left(\sqrt{\kappa^2 + \delta_\beta^2}\, z\right) e^{-\alpha z}. \tag{10}$$

Thus, the coupling efficiency η is obtained at the first peak, and the value is

$$\eta_{\max} = \frac{1}{1 + (\delta_\beta/\kappa)^2} e^{\left[-\alpha\pi/\left(2\sqrt{\delta_\beta^2+\kappa^2}\right)\right]}. \tag{11}$$

D. Mode-Coupling Bandwidth and Crosstalk

Equation (10) can be employed to evaluate the bandwidth of a coupler and crosstalk from undesired modes. The coupling efficiency η changes along frequency, and the bandwidth can be calculated when all the frequency-dependent parameters are extracted. The mode crosstalk can also be approximated with the mode characteristics. For instance, E_{11}^y and E_{31}^y modes are the undesired modes in an E_{11}^y–E_{21}^y coupler, but they do exist with large gap of δ_β, so the crosstalk to is relative low but worthy of attention.

The bandwidth of the DWG mode coupler is rarely discussed in publications, because DWGs, such as fibers, are mainly applied in the optic domain and have sufficient absolute bandwidth [28] because of the ultrahigh carrier frequency. However, the bandwidth could be a bottleneck when it is applied in sub-THz/THz bands due to the limited fractional bandwidth. Fig. 7 shows frequency-dependent parameters of a rectangular DWG coupler, such as the effective refractive index n_{eff} in Fig. 7(a), coupling coefficient in Fig. 7(b), and δ_β^2/κ^2 ratio in Fig. 7(c) that determines the coupling efficiency factor F. At last, according to (8), the optimum coupler length L_C is normally selected for the center frequency based on δ_β and κ. All of the parameters together determine the coupling efficiency at different frequencies and then decide the bandwidth. The effective refractive index n_{eff} dependency on frequency makes the propagation constant $\beta = n_{\text{eff}} \cdot \omega/c$ have a higher-order relation to the frequency. β describes the propagation characteristics and has influence on all the other parameters, among which the coupling coefficient κ and propagation constant difference δ_β are the most significant factors that affect the mode-coupling bandwidth.

For E_{11}^y–E_{11}^y mode coupler, the modes and dimensions of the waveguides are identical; thus, δ_β is always zero, and the coupling efficiency factor F is always one at any frequency, as shown in Fig. 8(a). However, L_C varies with frequency, because κ is a frequency-dependent variable, and the corresponding optimum coupler length varies from 3.1 to 4.8 mm in the frequency band of 140–190 GHz. If the optimum coupler length $L_C = 3.8$ mm at the center frequency of 165 GHz is picked, the maximum $\eta = 0.92$ is achieved after taking the material loss into account, and it drops to 0.81 at the edges of the band (140 and 190 GHz).

For E_{11}^y–E_{21}^y and E_{11}^y–E_{31}^y mode couplers, ideal phase matching condition can only be satisfied at the center frequency, as shown in Fig. 7(c). The increasing δ_β not only reduces the achievable maximum coupling efficiency F, but also makes the optimum coupler length L_C be a stronger frequency-dependent variable, thus leading to a smaller bandwidth. Fig. 8(b) and (c) clearly dictates the bandwidth degradation in the E_{11}^y–E_{21}^y and E_{11}^y–E_{31}^y mode couplers. At the edges of the frequency band (140 and 190 GHz), F drops to 0.95 and 0.91 due to nonzero δ_β; then, η is further reduced

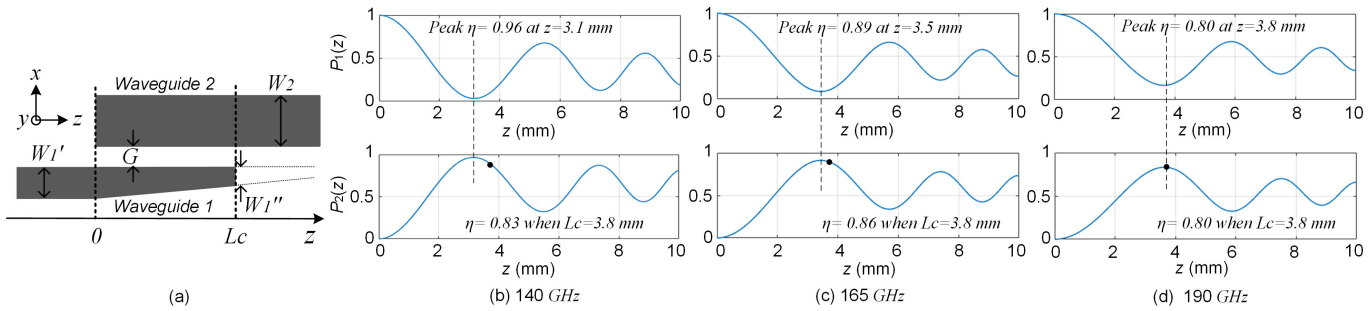

Fig. 9. (a) Geometry illustration of a one-side tapered DWG coupler. Calculated power intensity $P_1(z)$ in waveguide 1 and $P_2(z)$ waveguide 2 for the one-side tapered E_{11}^y–E_{21}^y coupler at (b) 140, (c) 165, and (d) 190 GHz.

to 0.78 and 0.70 because of the nonoptimum coupler length. The bandwidth degradation caused by β mismatch is more significant in the coupling between modes with larger order difference, such as E_{11}^y and E_{31}^y.

The mode crosstalk is also evaluated with (10). For the E_{11}^y–E_{11}^y coupler with a width of $W_1 = W_2 = 300$ μm, only the fundamental mode exists in the DWGs; thus, the crosstalk from higher-order modes is negligible, as shown in Fig. 8(a). For a DWG in larger width of $W_2 = 760$ or 1200 μm, multiple modes (E_{11}^y, E_{21}^y, and E_{31}^y) can coexist together in the DWG. Therefore, the crosstalk between undesired mode coupling occurs, and it can also be qualified by substituting the corresponding κ and β into (10). For instance, E_{11}^y and E_{31}^y are undesired in the wider arm (760 μm) of the E_{11}^y–E_{21}^y coupler, but E_{11}^y is still transferred into E_{11}^y and E_{31}^y, which causes the mode crosstalk. Since β for the undesired modes is usually unmatched, the crosstalk is in low coupling efficiency. The calculated in-band crosstalk from all other mode is less than 0.14% (−28.5 dB), as shown in Fig. 8(b) and (c).

E. Bandwidth Improvement: One-Side Tapered Coupler

As mentioned before, most of the parameters of the mode couple are frequency-dependent, which leads to the variation of the coupling efficiency with frequency and constrains the bandwidth. The β mismatching producing negative influence to the bandwidth must be reduced for bandwidth enhancement.

A one-side tapered structure with $W_1' = 340$ μm and $W_1'' = 260$ μm is designed, as shown in Fig. 9(a), to provide a wider n_{eff} coverage. In the frequency range from 140 to 190 GHz, the n_{eff} for E_{11}^y mode in the uniform-width DWG has a range of 2.41–2.64, while the n_{eff} in the one-side tapered coupler varies in a range of 2.31–2.72, which covers the n_{eff} range of 2.34–2.68 for E_{21}^y mode in a 760-μm-wide DWG and n_{eff} range of 2.31–2.70 for E_{31}^y mode in a 1200-μm-wide DWG. Therefore, a tapered structure can match the propagation constant in a wider frequency range, thus increasing the bandwidth. Besides that, one-side tapered coupler helps the EM wave coupling from the inner side, which is beneficial to coupling efficiency.

To theoretically verify the performance of one-side tapered coupler structure, an accurate mathematical model is required. Different from uniform-width coupler, not only the EM field magnitude $A(z)$ and $B(z)$, but also $\kappa(z)$ and $\delta_\beta(z)$ are the functions in terms of z in a tapered coupler. Therefore, the

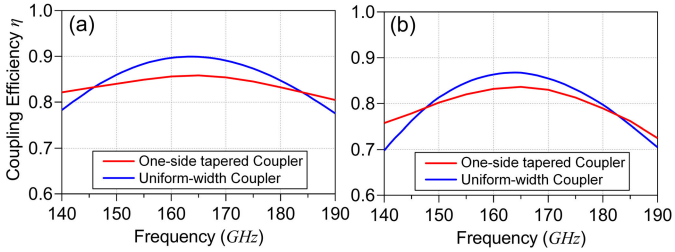

Fig. 10. Calculated bandwidth comparison between the one-side tapered and uniform-width structures for (a) E_{11}^y–E_{21}^y coupler and (b) E_{11}^y–E_{31}^y coupler.

expression of $\mathrm{d}A(z)/\mathrm{d}z$ and $\mathrm{d}B(z)/\mathrm{d}z$ becomes

$$\begin{cases} \dfrac{dA(z)}{dz} = -j\kappa(z)B(z)e^{[-j2\delta_\beta(z)z]} \\ \dfrac{dB(z)}{dz} = -j\kappa(z)A(z)e^{[j2\delta_\beta(z)z]}. \end{cases} \tag{12}$$

The higher-order differential equations are difficult to obtain an analytical solution. Fortunately, with technical computing tools, such as Mathematica, we are able to solve and plot numerical solutions with the initial condition in (5). First, a $W - z$ coordinate system is established according to Fig. 9(a) by two points $W_1' = 340$ μm at $z = 0$ and $W_1'' = 260$ μm at $z = Lc = 3.8$ mm. Since all the parameters, including n_{eff}, κ, and δ_β, have been extracted or calculated, as shown in Figs. 3 and 7, and they are correlated with the mode and DWG width W at a specific frequency, we are able to fit the functions of $\kappa(z)$ and $\delta_\beta(z)$ in the $W - z$ coordinate.

Taking E_{11}^y–E_{21}^y coupler as an example, the fitting functions of $\kappa(z)$ and $\delta_\beta(z)$ in (13) are obtained at 165 GHz in unit of millimeter

$$\begin{cases} \kappa(z) = -3.217 \times 10^{-6} \cdot z + 0.415 \\ 2\delta_\beta(z) = \dfrac{\omega}{c}(-0.085 \cdot z + 0.152). \end{cases} \tag{13}$$

In a small width range of 260–340 μm, $\delta_\beta(z)$ can be considered to be linear to z, and $\kappa(z)$ is a weak function of z, because the coupler's gap is fixed. Plugging (13) into (12), the numerical solutions of $A(z)$, $B(z)$, $P_1(z)$, and $\eta = P_2(z)$ can be solved. This approach is also applied to the other frequencies; then, $P_1(z)$ and $P_2(z)$ at 140, 165, and 190 GHz are solved and plotted in Fig. 9(b)–(d), respectively. With the same coupler length ($z = Lc = 3.8$ mm), the one-side

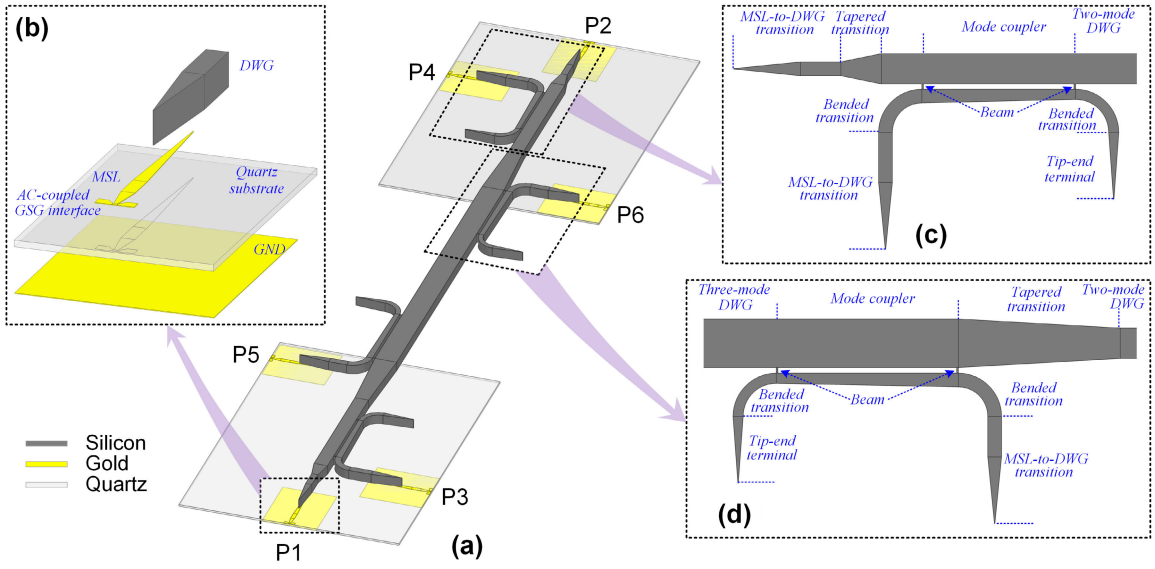

Fig. 11. (a) 3-D view of the multimode multidrop Si DWG channel, (b) MSL-to-DWG transition, (c) E_{11}^y–E_{21}^y coupler, and (d) E_{11}^y–E_{31}^y coupler.

tapered E_{11}^y–E_{21}^y coupler archives more even coupling efficiency over the frequency, because the maximum coupling efficiency factor F and the optimum coupler length Lc are split to different frequencies. The bandwidth performance between one-side tapered and uniform-width structures for E_{11}^y–E_{21}^y and E_{11}^y–E_{31}^y couplers is compared in Fig. 10. The bandwidth performance is significantly improved with a drawback that the maximum coupling efficiency at the center frequency is degraded by about 0.3 dB.

III. Multimode Multidrop Si DWG Design and Fabrication

The design, optimization, fabrication process, and packaging procedures of the proposed multimode multidrop Si DWG channel will be introduced in this section. As shown in Fig. 11(a), the entire structure cascades microstrip line (MSL)-to-DWG transition (quasi-TEM to E_{11}^y mode coupler), E_{11}^y–E_{21}^y and E_{11}^y–E_{31}^y mode couplers, and a multimode Si DWG in the center, and it enables three individual signal transmissions simultaneously. High-resistivity Si is employed as the dielectric material to fabricate the compact DWG channel because of the high permittivity and low loss tangent. The bidirectional structure has six ports to excite and (de)multiplex E_{11}^y (P1 and P2), E_{21}^y (P3 and P4), and E_{31}^y (P5 and P6), respectively, and independently. Two (de)multiplexers are assembled on each side of the channel. Three types of mode couplers construct the (de)multiplexer, as shown in Fig. 11(b)–(d). The MSL-to-DWG transitions are fabricated on a 100-μm-thick quartz substrate ($\varepsilon_r = 3.78$ and $\tan\delta = 0.0001$). It generates and feeds E_{11}^y mode to all the ports of multidrop Si DWG. E_{11}^y–E_{21}^y and E_{11}^y–E_{31}^y mode couplers convert E_{11}^y to higher-order modes at P3 and P5 (or P4 and P6); then, three modes are generated, combined, and transmitted in the shared common waveguide in the center.

A. Multimode Si DWG Bus and MSL-to-DWG Transition

The common section of the channel is a multimode Si DWG that should support multiple modes simultaneously. The propagation of y-polarization modes, such as E_{11}^y, E_{21}^y, and E_{31}^y, is mainly determined by the waveguide width, as discussed in Section II. E_{11}^y, E_{21}^y, and E_{31}^y can coexist simultaneously when the DWG width is larger than 620 μm according to Fig. 3. However, to support phase matching for E_{31}^y to E_{11}^y in the DWG coupler arm with a width of 300 μm, the width of 1200 μm is selected. DWG's height is not critical for y-polarization planar waves in horizontal couplers. Considering the operation frequency and fabrication complexity, a Si wafer with a thickness of 525 μm is chosen to etch through and forms the DWG structure.

This channel is designed to bridge CMOS transmitter (TX) and receiver (RX) chipsets, and MSL is one of the widely used interfaces in RF, mm-wave, and THz systems. Therefore, the MSL-to-DWG transitions (quasi-TEM to E_{11}^y coupler) with a commercial 50-Ω ground–signal–ground (GSG) interface are necessary for measurement and system integration. Fig. 11(a) shows the configuration of the MSL-to-DWG transition, and it smoothly transfers the quasi-TEM mode in an MSL to E_{11}^y in a rectangular DWG with the minimum insertion loss of 1.8- and 3-dB bandwidth of 83 GHz. Since the structure has been successfully demonstrated and introduced in [29] and [30], it will not be repeated in this article.

B. One-Side Tapered DWG Mode Coupler

In actual coupler design, the first step is to minimize the propagation constant difference δ_β at the center frequency by tuning the width of DWGs and then select the optimum coupler length L_C. To reduce the channel loss and coupler size, the first peak at $m = 0$ is usually preferred according to (8). Besides the frequency-dependent parameters in mode couplers, the waveguide cutoff frequency, undesired mode conversion at high frequency, and reflection also constrain the overall bandwidth. Therefore, the bandwidth in practice will be smaller than the theoretical calculation.

Fig. 11(c) and (d) depicts the structures of one-side tapered E_{11}^y–E_{21}^y and E_{11}^y–E_{31}^y couplers. The n_{eff} of mode E_{11}^y in a 300-μm-wide Si DWG is 2.54 at 165 GHz, which equals the n_{eff}

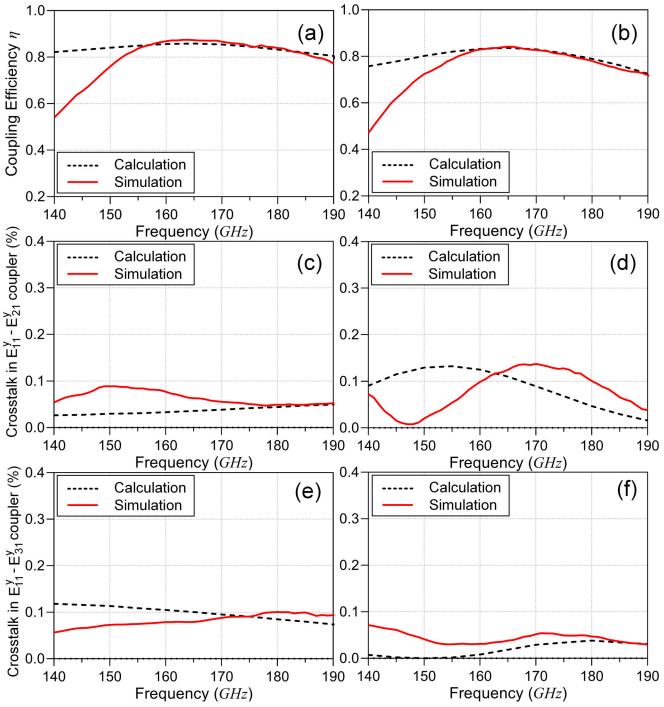

Fig. 12. Calculated and simulated performance of one-side tapered mode couplers. Coupling efficiency of (a) E_{11}^y–E_{21}^y and (b) E_{11}^y–E_{31}^y couplers. Crosstalk from (c) E_{11}^y and (d) E_{31}^y modes in E_{11}^y–E_{21}^y coupler. Crosstalk from (e) E_{11}^y and (f) E_{21}^y modes in E_{11}^y–E_{31}^y coupler.

of E_{21}^y in a 760-μm-wide DWG and E_{31}^y in a 1200-μm-wide DWG. Therefore, the initial widths of $W_1 = 300$ μm, $W_2 = 760$ μm, and $W_3 = 1200$ μm are selected for the coupler arms. The optimum L_C values of 3.8 and 4.3 mm are optimized for E_{11}^y–E_{21}^y and E_{11}^y–E_{31}^y mode couplers because of the different gaps of 130 and 140 μm are selected. Large gap is helpful to avoid undesired higher-order mode conversion, especially for more sensitive higher-order mode coupler, such as E_{11}^y–E_{31}^y coupler. E_{11}^y–E_{11}^y mode coupler is not adopted in the multidrop channel, while MSL-to-DWG transition is employed to transfer between E_{11}^y and quasi-TEM mode for the GSG interfaces.

One-side tapered coupler matches the β for wider frequency band and couples EM energy from the inner to the other coupler arm, thus minimizing EM energy waste. To comprehensively verify the performance of one-side tapered couplers, calculated results from Section III-B E are compared with HFSS simulations, as shown in Fig. 12. The calculation matches well with simulation at the high-frequency side, but discrepancy happens at low frequency due to the performance roll-off when close to the cutoff frequency of E_{21}^y and E_{31}^y modes, which is about 130 GHz. The roll-off phenomenon can be captured in HFSS simulation but not be included in equations. Fig. 12(c)–(f) depicts the calculated and simulated mode crosstalk in both E_{11}^y–E_{21}^y and E_{11}^y–E_{31}^y mode couplers, which are all lower than 0.14% (−28.5 dB). Similarly, the crosstalks match better at higher frequency.

The entire DWG mode-coupler structure is illustrated in Fig. 13. It consists of two parallel coupler arms with optimized width and gap to minimize δ_β. The coupler launching arm

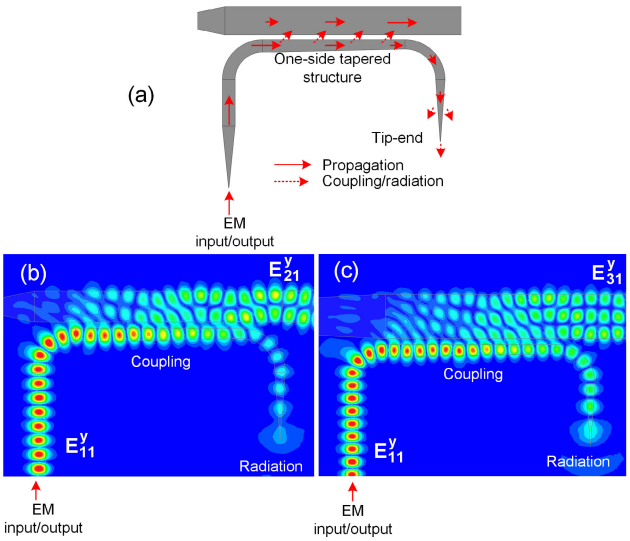

Fig. 13. (a) Entire structure of one-side tapered coupler. E-field distribution of (b) E_{11}^y–E_{21}^y and (c) E_{11}^y–E_{31}^y DWG mode couplers.

is in one-side tapered shape to enhance the bandwidth and terminated with a tip end. Large-radius bended DWGs are used to connect all the waveguide sections to smoothly guide the EM waves with negligible bending loss. The EM signal in E_{11}^y mode is injected to the DWG and then converted to E_{21}^y and E_{31}^y by the one-side tapered structure efficiently. The EM energy remaining in the coupler launching arm is guided to the tip-end terminal and radiated out of the waveguide. Otherwise, strong reflection at the coupler end will cause higher-order mode conversion and interference issues. The E-field distribution in Fig. 13(b) and (c) shows the smooth reciprocal mode coupling between E_{11}^y–E_{21}^y and E_{11}^y–E_{31}^y.

C. Tapered DWG Transition and Terminal

There are different types of tapers, such as one-side tapered DWG couplers, tip-end terminals, and taper transition between sections, employed in the multidrop Si DWG, as shown in Fig. 11. The light ray-tracing method provides an effective approach to analyze the planar waves inside a structure. The light ray-tracing method has been introduced to do guided mode solving in textbooks [24], [26], [27]. For planar waves ($k_x = 0$ or $k_y = 0$), the light beam is propagating along the wavenumber vector k_1 with an angle φ to the DWG inner surface, as shown in Fig. 14(a), and it can be calculated by

$$\cos\varphi = \frac{k_z}{k} = \frac{n_{\text{eff}}}{n_1}. \tag{14}$$

DWGs in different shapes, such as uniform-width, one-side tapered, and symmetric tapered DWGs, are shown in Fig. 14. For a guided wave propagating along the DWGs, the refractive index (n_1) of the core must be higher than the cladding's (n_0). Light rays are confined in the core by the total internal reflection condition as follows:

$$\varphi < (\pi/2 - \theta_c) \tag{15}$$

where θ_c is the critical angle $\theta_c = \arcsin(n_0/n_1)$.

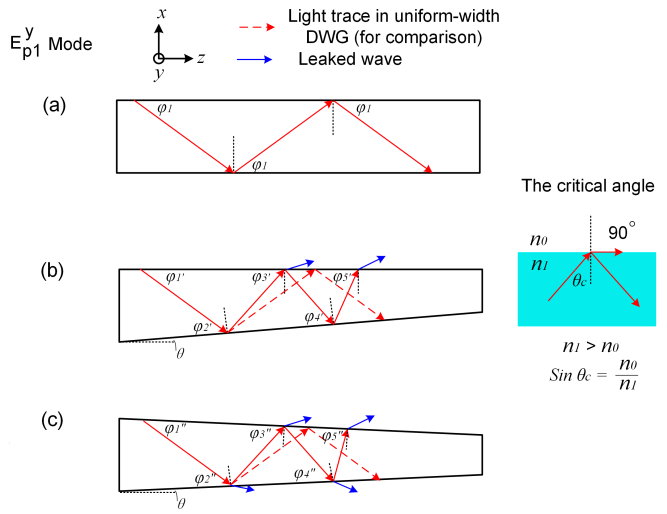

Fig. 14. Light ray trace in DWGs—(a) uniform-width, (b) one-side tapered, and (c) symmetric tapered DWGs.

For the one-side taper structure in Fig. 14(b), φ is always increased at the bottom inclined plane by 2θ compared with the last cycle. Assuming φ_1 is the angle in a uniform-width DWG and θ is the angle of inclination, φ_n' in the one-side taper can be calculated as follows: $\varphi_1' = \varphi_1$; $\varphi_2' = \varphi_1 - \theta$; $\varphi_3' = \varphi_1 + \theta$; $\varphi_4' = \varphi_1$; $\varphi_5' = \varphi_1 + 3\theta$; ... The angle on the top plane exceeds $(\pi/2 - \theta_c)$ faster than the one on the bottom plane. Therefore, EM waves tend to leak from the top plane in one-side tapers.

For the symmetric taper in Fig. 14(c), the angle φ_n'' is increasing more evenly and quickly. The angle changes as follows: $\varphi_1'' = \varphi_1 - \theta$; $\varphi_2'' = \varphi_1 + \theta$; $\varphi_3'' = \varphi_1 + 3\theta$; $\varphi_4'' = \varphi_1 + 5\theta$; $\varphi_5'' = \varphi_1 + 7\theta$; ... When φ_n'' exceeds $(\pi/2 - \theta_c)$, the EM waves start to leak from both sides evenly, which is the working mechanism of tipped terminals.

For the tapered transitions, normally, a small inclination angle is preferred to minimize the influence on the angle φ and avoid undesired mode conversions. A steep-slope taper would cause undesired mode conversion and extra EM wave leakage. If multiple modes are imported from the wider side, the taper can work as a mode filter to filter out the higher-order modes when the slope and length of the taper are designed properly.

D. Fabrication and Packaging

The Si channel and transition quartz board are fabricated in-house with nanomanufacturing processes. For the multimode multidrop Si DWG channel, all the parts including transitions, Si DWG and coupler arms, must be precisely aligned; thus, it is better to fabricate them in one whole piece to avoid alignment issues. For this purpose, several beams are utilized to connect the coupler arms with the multimode DWG together, as shown in Fig. 11. Two 40-μm-wide beams are sufficient to hold the coupler arm solidly and have little influence on the mode coupling. The multimode multidrop Si channel is produced by deep reactive ion-etching (DRIE) process. Since the Si wafer in a thickness of 525 μm needs to be etched through, larger exposed area is preferred, that is the reason why narrow gap in the coupler will cause etching problems.

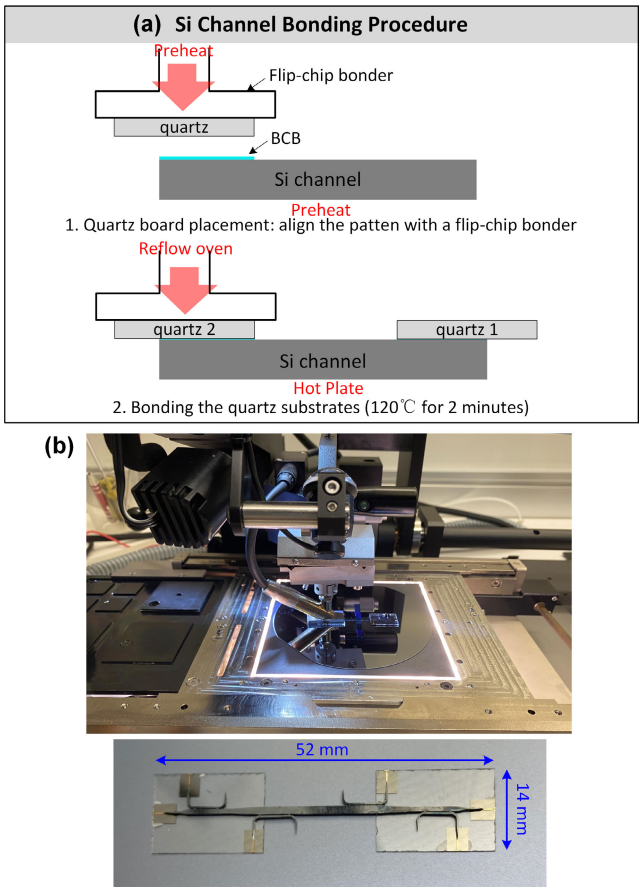

Fig. 15. (a) Multimode multidrop channel bonding procedure and (b) photographs of the process and sample.

To further enhance the mechanical strength, the Si DWG channel is better to sit on large transition boards and be bonded with strong glue. On the other hand, both the handling board (quartz: $\varepsilon_r = 3.78$) and bonding glue (BCB: $\varepsilon_r = 2.65$) should have relative low dielectric constant, so that they will not affect the mode coupling. Six MSL-to-DWG transitions are divided into two groups and fabricated on two pieces of 100-μm quartz substrates The transition traces are patterned with a Ti ($\sigma = 1.82 \times 10^6$ S/m)/Au ($\sigma = 4.1 \times 10^7$ S/m) thin film of thickness 50/300 nm using lithography, metal deposition, liftoff, and plating processes. The detailed fabrication processes are introduced in [3] and [29].

Customized packaging procedures are designed for the multimode multidrop Si DWG channel, as shown in Fig. 15(a). Quartz substrates are bonded toward the large-size DWG channel precisely by a flip-chip bonder. The bonding direction from quartz to Si DWG is beneficial to improve the bonding stability and accuracy. Preheating is a necessary step to reduce shaking during raising temperature process, because thermal expansion and contraction will cause undesired movement of samples. The bonding offset could be less than 5 μm if strictly following this process. The photographs of the bonding process and final Si DWG channel sample are shown in Fig. 15(b). To date, the entire multimode multidrop channel

is formed, and all the six ports are tied to GSG interfaces, so that the channel is ready to be measured with commercial RF probes on a testing station.

For the multimode multidrop channel-based sub-THz interconnect system, there are a few more procedures to assemble the CMOS TX/RX chips and mount the interconnect to a mother printed circuit board (PCB). The bonding sequence is determined by the thickness of components and temperature of reflow oven. The thin CMOS chips reacquiring the highest reflow oven temperature are flip-bonded to quartz substrates in the first place. Then, the quartz substrates with the CMOS chips are bonded to multimode multidrop channel, similar to the individual DWG channel boding process. After that, the sub-THz interconnect is mounted on a PCB together with surface mount device (SMD) and uses bonding wires to connect the baseband signal chains and dc supplies. The full package will be introduced in Section IV.

IV. Si DWG Channel and Sub-THz Interconnect System Demonstrations

A. Multimode Multidrop Si DWG Channel Measurement

The entire multimode multidrop Si DWG channel, including transition boards, is designed in full-wave simulator HFSS and measured on-wafer with G-band (140–220 GHz) testbenches. The Si DWG channel is connected with 100-μm pitch GSG pads, so it can be tested with standard RF probes. The measurement and characterization of sub-THz/THz DWGs have been investigated and compared in [7] and [31]. The performance of a stand-alone DWG, such as transmission loss, return loss, bandwidth, attenuation, and propagation constants, is worthy of evaluating and fully investigated in [29]. The major application of the proposed multimode multidrop channel is chip-to-chip communication, and it is better to measure the back-to-back S-parameters at the GSG port end, which is the exact channel characterization present to the TXs and RXs.

Two testbenches were set up to measure the multimode multidrop channel, as shown in Fig. 16. The G-band S-parameter testbench in Fig. 16(a) includes an Agilent network analyzer (PNA-X N5247A), a pair of Virginia Diodes frequency extension modules (VDI WR5.1-VNAX), WR-5 S-bend waveguides, and a pair of WR-5 probes. The short, open, load, thru (SOLT) calibration method is employed to set the reference plane at the probe tip, so that this is the most accurate bench for G-band S-parameter measurement. However, the old version of frequency extender station has a limit of rotation, which constrains the crosstalk measurement. For example, the crosstalk from E^y_{11} path to E^y_{31} path must be measured in north and west directions.

The second testbench that has more flexibility to rotate is the setup in Fig. 16(b). A signal generator (E8257D), a VDI WR5.1 tripler, a downconversion mixer, and a signal analyzer (PXA N9030B) were used for testing transition loss and port crosstalk, because this setup was flexible to rotate the probes appropriately to any directions, as shown in Fig. 16(d). A standard "through" calibration kit was used for cable and probe de-embedding in the testbench. Then, replacing the "through" calibration kit with the device under test (DUT), both the transition loss and crosstalk can be obtained accurately by comparing the power detected with the signal analyzer. The mismatch (or reflection) of the interface cannot be removed in this setup, but the error introduced is negligible, because both GSG interface and standard GSG probe have decent $S11$.

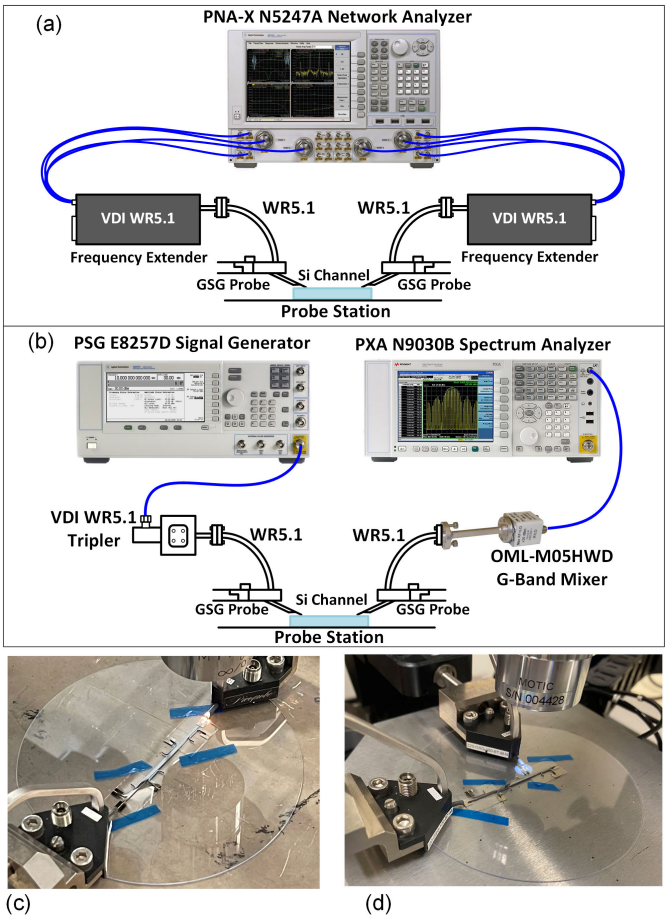

Fig. 16. Setup illustration for testing (a) S-parameters and (b) transition loss and crosstalk. Wafer-probe characterization of (c) transition loss and (d) crosstalk.

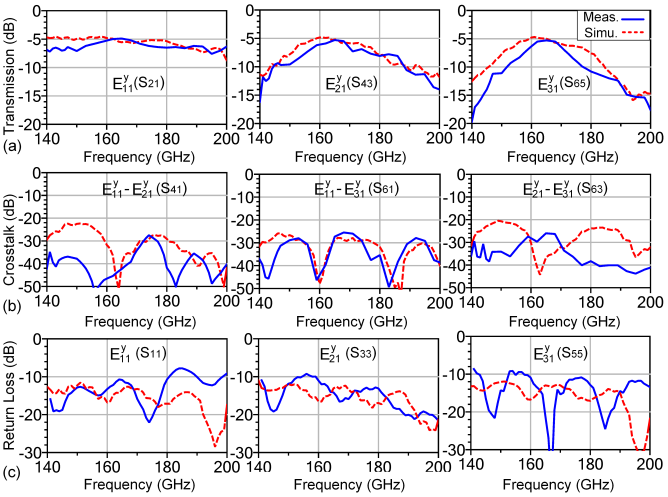

Fig. 17. Simulated and measured S-parameters of the multimode multidrop Si DWG channel—(a) transmission loss, (b) crosstalk, and (c) return loss.

TABLE I

COMPARISON WITH THE STATE-OF-THE-ART MULTICHANNEL TRANSMISSIONS AT mm-WAVE, SUB-THz, AND THz

	JSSC'11 [9]	TMTT'18 [21]	TMTT'20 [18]	IRMMW -THz'21 [20]	ISSCC'22 [16]	TTHz'22 [32]	This Work
3-dB Bandwidth (GHz)	57∼80	150.8∼206 151∼171.4	225∼250 [a] 262∼285 [a] 302∼322 [a]	127.7-152.3 168.3-191	40∼85	600∼637 630∼730	143∼200 151∼185 155∼174
Multi-Channel Scheme	FDM	MDM	FDM	FDM	Shield	FDM	MDM
Technique	Plastic	DWG	Ridged SIW	MSL	E-Tube	DWG	DWG
Numbers of Channels	2	2	3	2	2	2	3
Back-to-back Transmission Loss (dB)	7	6.4/6.6	6/8/10 [b]	11.6/13.2	13	0.24/1.08 [c]	5/5.1/5.3
In-band Crosstalk (dB)	-20	-20	-35	-30	-55	-10 [d]	-26

a. Read from the figure; *b*. the total loss of a multiplexer and demultiplexer; *c*. the insertion loss of the standalone DWG; *d*. at 630∼660 GHz.

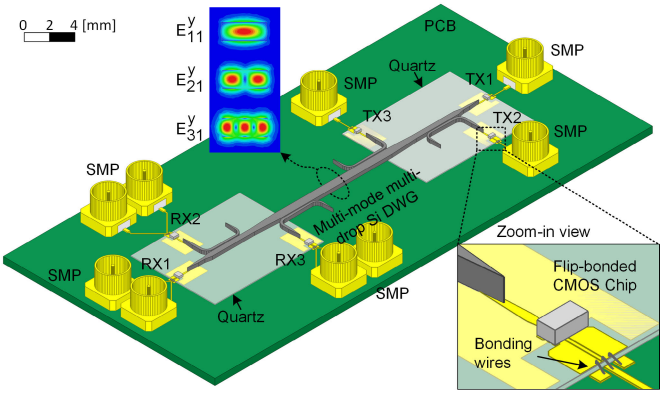

Fig. 18. Multimode multidrop sub-THz interconnect system implementation includes flip-bonded Si DWG channel, (de)multiplexers, CMOS TX/RX chips, and interfaces on PCB.

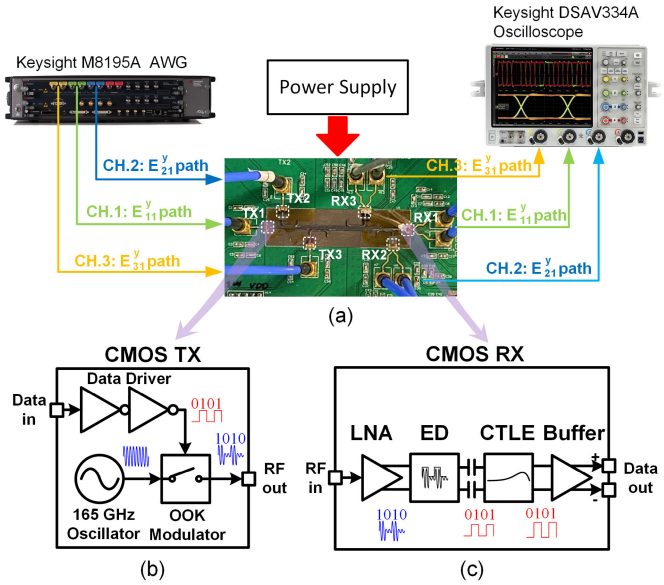

Fig. 19. (a) Testing setup of the multimode multidrop sub-THz interconnect system. Block diagrams of (b) TX and (c) RX.

The simulated and measured S-parameters of the multimode multidrop DWG channel across the observation bandwidth are plotted in Fig. 17. The minimum back-to-back transmission loss is about 5 dB within the 3-dB bandwidth of 143–200, 151–185, and 155–174 GHz for E_{11}^y path, E_{21}^y path, and E_{31}^y path, respectively. The proposed multimode multidrop channel provides more than 100-GHz bandwidth in total, which can support above 100-Gb/s data rate theoretically. Even though the three channels share the same physical link and frequency band, the measured mode crosstalk is all below −26 dB. Table I compares the results of the state-of-the-art (SOA) multichannel transmissions at mm-wave, sub-THz, and THz; [32] has good insertion loss and bandwidth performance for the individual DWG, but large in-band crosstalk will generate significant interference, which reveals that the proposed design achieves the maximum channels, minimum back-to-back transmission loss, and largest fractional bandwidth.

B. Sub-THz Interconnect System Demonstration

A multimode multidrop sub-THz interconnect system has been developed to evaluate the data capability of the Si DWG channel. The system, as depicted in Fig. 18, employs high-energy-efficiency active subsystems, such as on–off keying (OOK) TXs, and direct detection RXs, due to the channel's competitive transmission loss and bandwidth performance. The TX comprises an inverter-based data driver, a cross-coupled oscillator as the 165-GHz carrier generator, and a switch-based OOK modulator. On the other hand, the RX comprises a low-noise amplifier (LNA), an envelope detector (ED), a continuous time linear equalizer (CTLE), and a buffer. Both TX and RX chips have been fabricated in a 65-nm CMOS technology, with the dimensions of 0.38 × 0.72 and 0.65 × 0.77 mm^2, respectively. The detailed circuits design is elaborated in [33]. Pseudorandom binary sequence (PRBS) patterns of $2^{21} - 1$ are generated to test the data rate, eye diagram, and bathtub curve of the three modes simultaneously, as shown in Fig. 19. The OOK modulator and direct detection RX do not require any off-chip local oscillator (LO) and phase synchronization; therefore, the measurement configuration is straightforward.

Fig. 20 shows the measured waveform, eye diagrams, and bathtub curves of the three mode paths. The measured data rates for E_{11}^y, E_{21}^y, and E_{31}^y paths are 24, 22, and 19 Gb/s, respectively, with a bit error rate (BER) better than 10^{-12}. The demonstrated aggregate data rate of the three channels is 65 Gb/s with an energy efficiency of 1.6 pJ/b. The proposed multimode multidrop sub-THz interconnect system achieves the best energy efficiency with the capabilities to support multidrop and further scalability for a larger number of channels and ports.

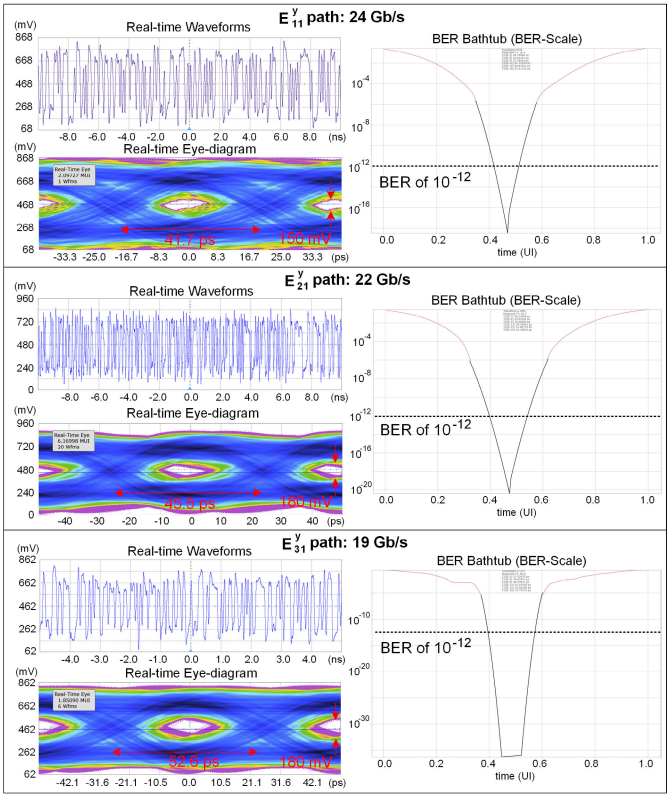

Fig. 20. Measured data rates, waveform, eye diagrams, and bathtub curves of the E_{11}^{y}, E_{21}^{y}, and E_{31}^{y} paths in simultaneous data transmission.

V. Conclusion

This article presents a mode-coupler-based multimode multidrop Si DWG at *G*-band with the design, analysis, and demonstration elaborated. To the best of our knowledge, this is the first time three-MDM-based channelization demonstrated on a DWG. The design method can be extended to more modes, allowing for more channels per physical link to materialize high bandwidth density and high energy efficiency multidrop sub-THz/THz interconnect, and meet the growing interconnect demands. It is important to note that the demonstration channel length of 5.2 cm was due to the size constraint of the wafer used to fabricate the channel. This interconnect system can be readily extended to the meter range due to the channel ultralow loss feature ($\tan\delta = 0.003$). Besides, with more advanced semiconductor technologies for active circuits, the data rate per channel will be further increased. Therefore, we believe that the demonstrated multimode multidrop sub-THz interconnect scheme opens a new path with high potentials to complement the existing electrical and optical interconnects to address the challenging meter range wireline communication scenarios.

Acknowledgment

The authors would like to thank Dr. Bo Yu at Apple Inc., San Diego, CA, USA, for critical discussions, the Center for Nano and Micro Manufacturing (CNM2), UC Davis, CA, USA, for components fabrication, and the Davis Millimeter-Wave Research Center (DMRC), UC Davis, CA, USA, for measurements.

References

[1] Q. J. Gu, "Sub-THz/THz interconnect, complement to electrical and optical interconnects: Addressing fundamental challenges related to communication distances," *IEEE Solid StateCircuits Mag.*, vol. 12, no. 4, pp. 20–32, Fall 2020.

[2] Q. J. Gu, B. Yu, X. Ding, Y. Ye, X. Liu, and Z. Xu, "THz interconnect for inter-/intra-chip communication," in *Proc. SPIE*, vol. 10982, 2019, Art. no. 109822R.

[3] B. Yu, Y. Liu, Y. Ye, J. Ren, X. Liu, and Q. J. Gu, "High-efficiency micromachined sub-THz channels for low-cost interconnect for planar integrated circuits," *IEEE Trans. Microw. Theory Techn.*, vol. 64, no. 1, pp. 96–105, Jan. 2016.

[4] J. W. Holloway, L. Boglione, T. M. Hancock, and R. Han, "A fully integrated broadband sub-mmWave chip-to-chip interconnect," *IEEE Trans. Microw. Theory Techn.*, vol. 65, no. 7, pp. 2373–2386, Jul. 2017.

[5] J. W. Holloway, G. C. Dogiamis, and R. Han, "Innovations in terahertz interconnects: High-speed data transport over fully electrical terahertz waveguide links," *IEEE Microw. Mag.*, vol. 21, no. 1, pp. 35–50, Jan. 2020.

[6] B. Yu et al., "Sub-THz interconnect for planar chip-to-chip communications," in *Proc. IEEE 18th Topical Meeting Silicon Monolithic Integr. Circuits RF Syst. (SiRF)*, Jan. 2018, pp. 54–56.

[7] H. Zhu, Q. Xue, J. Hui, and S. W. Pang, "Design, fabrication, and measurement of the low-loss SOI-based dielectric microstrip line and its components," *IEEE Trans. Terahertz Sci. Technol.*, vol. 6, no. 5, pp. 696–705, Sep. 2016.

[8] W. Gao et al., "Characteristics of effective-medium-clad dielectric waveguides," *IEEE Trans. Terahertz Sci. Technol.*, vol. 11, no. 1, pp. 28–41, Jan. 2021.

[9] S. Fukuda et al., "A 12.5+12.5 Gb/s full-duplex plastic waveguide interconnect," *IEEE J. Solid-State Circuits*, vol. 46, no. 12, pp. 3113–3125, Dec. 2011.

[10] Y. Ye, B. Yu, X. Ding, X. Liu, and Q. J. Gu, "High energy-efficiency high bandwidth-density sub-THz interconnect for the 'last-centimeter' chip-to-chip communications," in *IEEE MTT-S Int. Microw. Symp. Dig.*, Jun. 2017, pp. 805–808.

[11] M. De Wit, Y. Zhang, and P. Reynaert, "Analysis and design of a foam-cladded PMF link with phase tuning in 28-nm CMOS," *IEEE J. Solid-State Circuits*, vol. 54, no. 7, pp. 1960–1969, Jul. 2019.

[12] Y. Kim et al., "150-GHz CMOS TX/RX with digitally predistorted PAM-4 modulation for terahertz contactless/plastic waveguide communications," *IEEE Trans. THz. Sci. Technol.*, vol. 10, no. 4, pp. 370–382, Jul. 2020.

[13] K. Dens, J. Vaes, S. Ooms, M. Wagner, and P. Reynaert, "A PAM4 dielectric waveguide link in 28 nm CMOS," in *Proc. IEEE 47th Eur. Solid State Circuits Conf. (ESSCIRC)*, Sep. 2021, pp. 479–482.

[14] P. J. Winzer, "Making spatial multiplexing a reality," *Nature Photon.*, vol. 8, no. 5, pp. 345–348, May 2014.

[15] X. Ding, B. Yu, H. Yu, S. S. Saber, and Q. J. Gu, "Multiplexing schemes for sub-THz/THz interconnects (invited)," in *Proc. IEEE Int. Symp. Radio-Frequency Integr. Technol. (RFIT)*, Aug. 2022, pp. 18–20.

[16] H. Song et al., "A 50 Gb/s PAM-4 bi-directional plastic waveguide link with carrier synchronization using PI-based Costas loop," in *IEEE Int. Solid-State Circuits Conf. (ISSCC) Dig. Tech. Papers*, vol. 65, Feb. 2022, pp. 1–3.

[17] U. Dey and J. Hesselbarth, "Building blocks for a millimeter-wave multiport multicast chip-to-chip interconnect based on dielectric waveguides," *IEEE Trans. Microw. Theory Techn.*, vol. 66, no. 12, pp. 5508–5520, Dec. 2018.

[18] J. W. Holloway, G. C. Dogiamis, S. Shin, and R. Han, "220-to-330-GHz manifold triplexer with wide stopband utilizing ridged substrate integrated waveguides," *IEEE Trans. Microw. Theory Techn.*, vol. 68, no. 8, pp. 3428–3438, Aug. 2020.

[19] J. W. Holloway, G. C. Dogiamis, and R. Han, "A 105 Gb/s dielectric-waveguide link in 130 nm BiCMOS using channelized 220-to-335 GHz signal and integrated waveguide coupler," in *IEEE Int. Solid-State Circuits Conf. (ISSCC) Dig. Tech. Papers*, vol. 64, Feb. 2021, pp. 196–198.

[20] X. Ding, B. Yu, Y. Ye, H. Yu, Z. Xu, and Q. Jane Gu, "An FDD-based full-duplex sub-THz interconnect with data-rate of 22.6 Gb/s and energy-efficiency of 1.58 pJ/bit," in *Proc. 46th Int. Conf. Infr., Millim. Terahertz Waves (IRMMW-THz)*, Aug. 2021, pp. 1–2.

[21] B. Yu et al., "Ortho-mode sub-THz interconnect channel for planar chip-to-chip communications," *IEEE Trans. Microw. Theory Techn.*, vol. 66, no. 4, pp. 1864–1873, Apr. 2018.

[22] N. Van Thienen, Y. Zhang, and P. Reynaert, "Bidirectional communication circuits for a 120-GHz PMF data link in 40-nm CMOS," *IEEE J. Solid-State Circuits*, vol. 53, no. 7, pp. 2023–2031, Jul. 2018.

[23] S. Moon and D. Y. Kim, "Effective single-mode transmission at wavelengths shorter than the cutoff wavelength of an optical fiber," *IEEE Photon. Technol. Lett.*, vol. 17, no. 12, pp. 2604–2606, Nov. 21, 2005.

[24] S. Chuang, *Physics of Photonic Devices* (Wiley Series in Pure and Applied Optics). Hoboken, NJ, USA: Wiley, 2009.

[25] C. Bender and S. Orszag, *Advanced Mathematical Methods for Scientists and Engineers I: Asymptotic Methods and Perturbation Theory*. New York, NY, USA: Springer, 2013.

[26] K. Okamoto, *Fundamentals of Optical Waveguides*. Amsterdam, The Netherlands: Elsevier Science, 2021.

[27] D. Pozar, *Microwave Engineering*, 4th ed. Hoboken, NJ, USA: Wiley, 2011.

[28] D. Dai and J. E. Bowers, "Novel concept for ultracompact polarization splitter-rotator based on silicon nanowires," *Opt. Exp.*, vol. 19, no. 11, pp. 10940–10949, 2011.

[29] B. Yu, Y. Liu, Y. Ye, X. Liu, and Q. J. Gu, "Low-loss and broadband G-band dielectric interconnect for chip-to-chip communication," *IEEE Microw. Wireless Compon. Lett.*, vol. 26, no. 7, pp. 478–480, Jul. 2016.

[30] X. Ding, H. Yu, S. Sabbaghi, and Q. J. Gu, "G-band mode-coupler-based Si dielectric waveguide for multidrop sub-THz interconnect," *IEEE Microw. Wireless Technol. Lett.*, vol. 33, no. 6, pp. 1–4, Jun. 2023.

[31] H. Zhu, J. Gauthier, and K. Wu, "Silicon probe measurement and characterization in sub-THz range," *IEEE Trans. Terahertz Sci. Technol.*, vol. 10, no. 6, pp. 606–616, Nov. 2020.

[32] N. Shibata, Y. Uemura, Y. Kawamoto, L. Yi, M. Fujita, and T. Nagatsuma, "Silicon dielectric diplexer module for 600-GHz-band frequency-division multiplexing wireless communication," *IEEE Trans. Terahertz Sci. Technol.*, vol. 12, no. 4, pp. 334–344, Jul. 2022.

[33] X. Ding, H. Yu, S. Sabbaghi, and Q. J. Gu, "A 1.6 pJ/b 65 Gb/s Si-dielectric-waveguide based multi-mode multi-drop sub-THz interconnect in 65 nm CMOS," in *Proc. IEEE Custom Integr. Circuits Conf. (CICC)*, Apr. 2023, pp. 1–2.

Xuan Ding (Member, IEEE) received the B.S. and M.S. (Hons.) degrees in electrical engineering from the University of Electronic Science and Technology of China (UESTC), Chengdu, China, in 2010 and 2013, respectively. He is currently pursuing the Ph.D. degree in electrical engineering at the University of California at Davis (UC Davis), Davis, CA, USA.

He is with the High-Speed Integrated Circuits and Systems Laboratory, UC Davis. His research interests include RF, microwave, and THz-integrated circuits and systems.

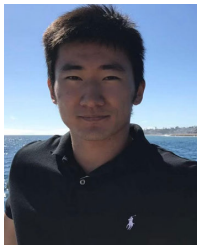

Hai Yu (Member, IEEE) received the B.S. degree in mechatronics engineering from the Beijing Institute of Technology, Beijing, China, in 2013, and the M.S. degree in electrical engineering from The Ohio State University, Columbus, OH, USA, in 2015. He is currently pursuing the Ph.D. degree in electrical engineering at the University of California at Davis, Davis, CA, USA.

His research interests include sub-THz sensing and transceivers.

Dr. Yu was a first-author recipient of the Best Student Paper Award at the 2020 IEEE International Microwave Symposium (IMS).

Sajjad Sabbaghi (Graduate Student Member, IEEE) received the B.S. degree in electronic engineering from Kashan University, Kashan, Iran, in 2015, and the master's degree in electronic engineering (IC design) from the K. N. Toosi University of Technology, Tehran, Iran, in 2018. He is currently pursuing the Ph.D. degree at the High-Speed Integrated Circuits and Systems Laboratory, University of California at Davis, Davis, CA, USA.

His research interests include millimeter-wave-integrated circuit design for sensing and communication applications.

Qun Jane Gu (Senior Member, IEEE) received the Ph.D. degree from the University of California at Los Angeles, Los Angeles, CA, USA, in 2007.

She is currently a Professor with the University of California at Davis (UC Davis), Davis, CA, USA. Her research interests include high efficiency, low-power interconnect, and millimeter-wave and sub-mm-wave/terahertz-integrated circuits and systems for communication, radar, and imaging.

Dr. Gu is a Technical Program Committee (TPC) member of solid-state circuits conferences, including IEEE Radio Frequency Integrated Circuits Symposium (RFIC), IEEE Custom Integrated Circuits Conference (CICC), and IEEE International Solid-State Circuits Conference (ISSCC). She was a recipient of the National Science Foundation (NSF) CAREER Award, the 2015 UC Davis Outstanding Junior Faculty Award, the 2017 and 2018 Qualcomm Faculty Award, the 2019 UC Davis Chancellor's Fellow, and the 2022–2023 IEEE Solid-State Circuits Society (SSCS) Distinguished Lecturer. Her group has got nine best paper awards from various international conferences. She was in the Steering Committee of International Microwave Symposium 2016 (IMS2016). She has been an Associate Editor of the IEEE MICROWAVE AND WIRELESS COMPONENTS LETTERS (MWCL) and the *Very Large-Scale Integration (VLSI) Journal of Integration*, and a Guest Editor of the IEEE JOURNAL OF SOLID-STATE CIRCUITS (JSSC) and the IEEE TRANSACTIONS ON MICROWAVE THEORY AND TECHNIQUES (T-MTT).